RESEARCH ARTICLE
SPACE PHYSICS

Earth and Planetary Physics
8: 1–14, 2024
doi: 10.26464/epp2023057

SMILE soft X-ray Imager flight model CCD370 pre-flight device characterisation

S. Parsons*, D. J. Hall, O. Hetherington, T. W. Buggey, T. Arnold, M. W. J. Hubbard, and A. Holland

Centre for Electronic Imaging, the Open University, Milton Keynes, MK7 6AA, UK

Key Points:

- Comprehensive preflight characterisation has taken place on the SMILE SXI flight grade CCDs.
- At the nominal operating temperature they all meet the procurement specifications.
- The baseline performance measurements provide a solid starting point for predicting how they will degrade through mission due to radiation damage.

Citation: Parsons, S., Hall, D. J., Hetherington, O., Buggey, T. W., Arnold, T., Hubbard, M. W. J., and Holland, A. (2024). SMILE soft X-ray Imager flight model CCD370 pre-flight device characterisation. *Earth Planet. Phys.*, *8*(1), 1–14. http://doi.org/10.26464/epp2023057

Abstract: Throughout the SMILE mission the satellite will be bombarded by radiation which gradually damages the focal plane devices and degrades their performance. In order to understand the changes of the CCD370s within the soft X-ray Imager, an initial characterisation of the devices has been carried out to give a baseline performance level. Three CCDs have been characterised, the two flight devices and the flight spare. This has been carried out at the Open University in a bespoke cleanroom measurement facility. The results show that there is a cluster of bright pixels in the flight spare which increases in size with temperature. However at the nominal operating temperature (−120 °C) it is within the procurement specifications. Overall, the devices meet the specifications when operating at −120 °C in 6 × 6 binned frame transfer science mode. The serial charge transfer inefficiency degrades with temperature in full frame mode. However any charge losses are recovered when binning/frame transfer is implemented.

Keywords: CCD; soft X-ray imager; characterisation; SMILE

1. Introduction

The Solar wind Magnetosphere Ionosphere Link Explorer (SMILE) is a joint mission between the European Space Agency (ESA) and the Chinese Academy of Sciences (CAS) that aims to observe the interaction between the solar wind and the magnetosphere on a global scale (Raab et al., 2016). The mission will use four instruments: a Soft X-ray Imager (SXI), a Ultra-Violet Imager (UVI), a Light Ion Analyser (LIA) and a Magnetometer (MAG). The SXI will observe the process of solar wind charge exchange, which generates low-energy 0.2–2.0 keV X-rays (Dennerl et al., 2012; Walsh et al., 2016). The SXI has two large CCD370s as its focal plane array, adapted from the CCD270s (CCD-Bruyeres) used on the PLATO mission and optimised to maximize their efficiency for low-flux, low-energy signals (Endicott et al., 2012). The improvement in performance is due to a supplementary buried channel and a boosted output amplifier, which increases responsivity and enables detection of smaller signals above the noise floor (Clarke et al., 2012; Seabroke et al., 2013).

SMILE will have a highly elliptical polar orbit. It will receive radiation damage from trapped and solar protons throughout its 3-year mission. Understanding the performance changes of the CCD370s within the SXI is crucial for the mission's success. Thus the initial performance and characteristics of the devices need to be well understood. The work presented in this paper provides baseline performance characteristics of the two SXI flight model CCDs and the flight spare. The tests have been carried out internally by the Open University.

The characterisation includes an assessment of the noise, spectral resolution, dark current, bright defects, charge injection structure uniformity, trap pumping for defect identification, X-ray charge transfer inefficiency (CTI) with an Fe-55 source and extended pixel edge response (EPER) CTI over a range of charge levels.

Results from testing the CCDs are evaluated against the SMILE SXI CCD procurement specifications (*SMILE CCD procurement specifications*, 2017). The specifications include some mismatching with the SMILE operating conditions, due to their PLATO heritage. The test conditions used throughout this campaign are intended to replicate, as closely as possible, conditions during the SMILE mission. Where these depart significantly from the procurement specification conditions the specifications/thresholds used for comparison against the measured results have been updated appropriately. Each specification has been assigned its own identifier e.g. CCD-RON-001-A in (*SMILE CCD procurement specifications*, 2017) and this convention has been maintained throughout this work for clarity.

Correspondence to: S. Parsons, steve.parsons@open.ac.uk
Received 11 APR 2023; Accepted 24 JUN 2023.
First Published online 14 AUG 2023.

2. Methodology

2.1 Devices Under Test

The three back illuminated 4510 × 4510 pixel CCD370s under test are manufactured by Teledyne-e2v. All have been identified as flight device quality. S/N 20122-13-01 (FM1) and S/N 20122-15-01 (FM2) are the flight models and S/N 20122-16-01 (FS) is the flight spare. Due to their size each device comes from a different wafer, however, all three are from the same production batch which provides added consistency in their build. The specifications are summarised in Table 1.

Table 1. CCD370 design specifications.

Specification	Values
Device	CCD370
Manufacturing company	Teledyne-e2v
Silicon substrate	SiC
Image area size	3791 rows × 4510 columns
Store area size	719 rows × 4510 columns
Native pixel size	18 µm × 18 µm
Sensitive silicon thickness	16 µm
Serial registers	1
Noise (4 MHz)	13 e^- rms
Dark signal (203 K)	0.5 e^-/pix/s
Output nodes	2
Full well capacity	850 ke^-
SBC capacity	20 ke^-
Output amplifier responsivity	7 µV/e^-

2.2 Experimental Setup

A vacuum chamber was used to carry out the characterisation of the CCDs, enabling cooling between −125 to −85 °C for the devices. X-ray measurements were conducted using a retractable Fe-55 source. A 1 mm aluminum plate was used to shield the store region. Figure 1 shows an image of one of the CCD370s mounted to the cold head. Further details describing a similar set up can be found in (Parsons et al., 2021).

2.3 Readout Schemes

The devices are run at a 100 kHz readout (pixel) speed; the parallel forward (without charge injection) for frame transfer and full frame used throughout the characterisation tests is shown in Figure 2 and Figure 3 respectively.

In full frame mode the device is read out by transferring all rows in the image and store area down one, and then carrying out a serial read consisting of 2255 serial transfers in each node to create an output image of 4510 × 4510 pixels (plus 50 columns of serial and 110 rows of parallel overscan).

In frame transfer mode the image is 6 × 6 binned; the parallel binning occurs at the image-store boundary where the 3791 image rows are moved into the store to occupy 632 rows. As the store region consists of 719 rows, the last 87 rows read out are binned overscan. In the same way it will, in-flight, the image area is integrated while the store region is read out, as illustrated in Figure 4.

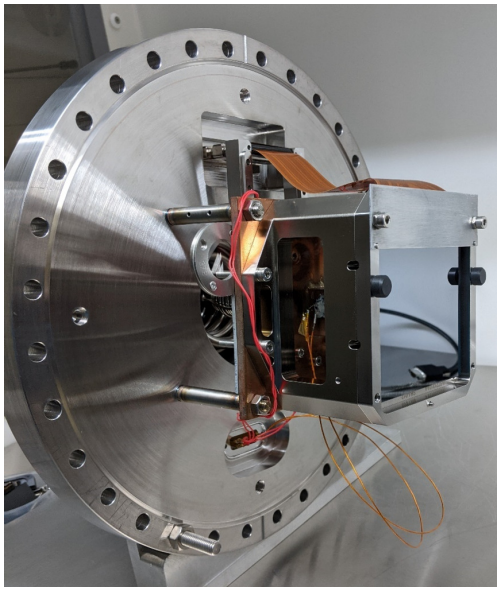

Figure 1. CCD370 installed onto chamber cold bench with shield covering store region.

In the serial readout, the pixels are binned into the summing well before being transferred onto the sense node, as shown in Figure 5. The serial can either be read out in burst mode where the reset and signal level sampling occurs separately to the serial clocking (which improves noise), or in video mode where they happen simultaneously, giving the opportunity to change/optimise the clocking speed and thus improve CTI. The testing has been carried out in burst mode as this is currently baselined for flight, and sampling window times are set to as long as possible while still maintaining the 100 kHz readout.

3. Characterisation Results

3.1 Noise

The system/image noise has been measured by extracting the standard deviation from a gaussian fit to the noise peak. System noise includes all sources of noise; the electronics noise has been measured separately with the CCD disconnected and is approximately 2 e^- rms.

The procurement reference is CCD-RON-001-A, which states that the readout noise BOL shall be lower or equal to 28 e^- rms (TBC) when measured single ended (Dummy outputs not used) with correlated double sampling and a bandwidth limitation of 15 MHz and a conversion gain of 7 µV/e (*SMILE CCD procurement specifications*, 2017). As these tests have been carried out with a readout speed significantly lower than 15 MHz, a 5 e^- rms readout noise limit will be assumed.

The results show that, when measured in serial overscan, the noise meets the requirements in both full frame, Figure 6, and frame transfer, Figure 7, readout modes.

The noise in the image areas has also been measured, primarily to see the effects of binning in the frame transfer images. The results

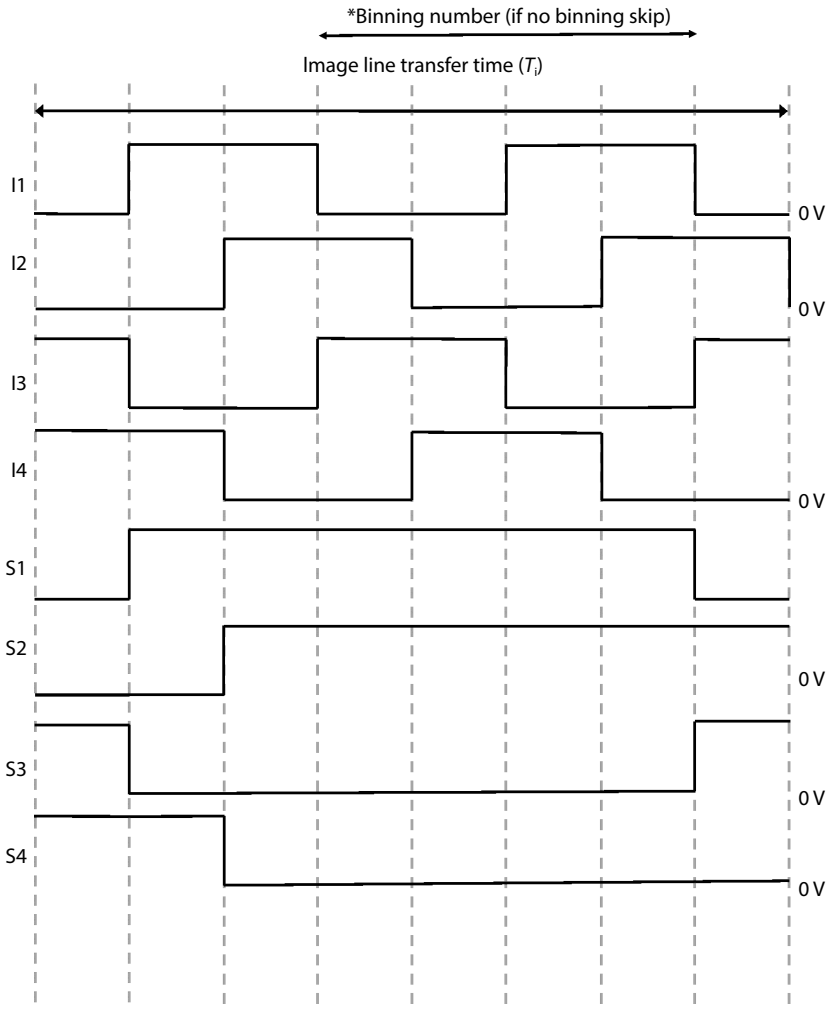

Figure 2. Frame Transfer parallel forward clocking scheme showing Image (I 1–4) and Store (S 1–4) clock sequences.

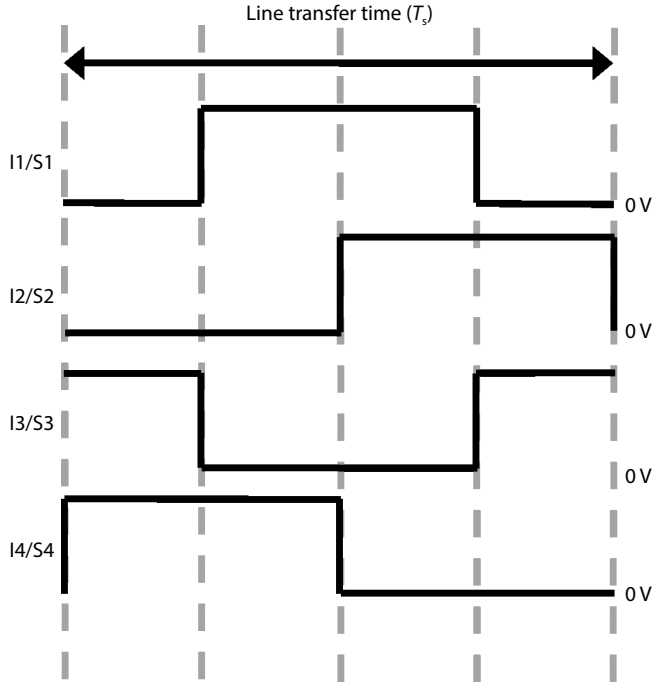

Figure 3. Full frame parallel forward clocking scheme showing Image (I 1–4) and Store (S 1–4) clock sequences.

show that it is consistently at least 1 e^- rms higher, and gradually increases above −100 °C in both readout modes. It is believed that the temperature dependent increase is due to dark current (DC), as it matches up with the results in Section 3.3. However this can not explain the 1 e^- rms increase across the temperature range, as the DC is not high enough to cause this at lower temperatures. Investigations are currently ongoing to determine the cause. However it is most likely related to the test system, as it has not been seen in other test campaigns carried out by ESA.

There is no variation between the devices within error. When accounting for the 2 e^- electronics noise and subtracting it in quadrature, the CCD noise is between 3.5–4.5 e^- rms.

3.2 Spectral Resolution

The resolution has been measured by fitting a Gaussian to isolated Fe-55 5.89 keV Kα X-rays and recording the Full Width Half Maximum (FWHM).

There is no defined requirement. However the X-ray instrument on SWIFT XRT (Pagani et al., 2011) had an FWHM of 150 eV and this is the assumed baseline.

The results show that across the majority of the assessed temperature range the resolution does not vary outside of error with

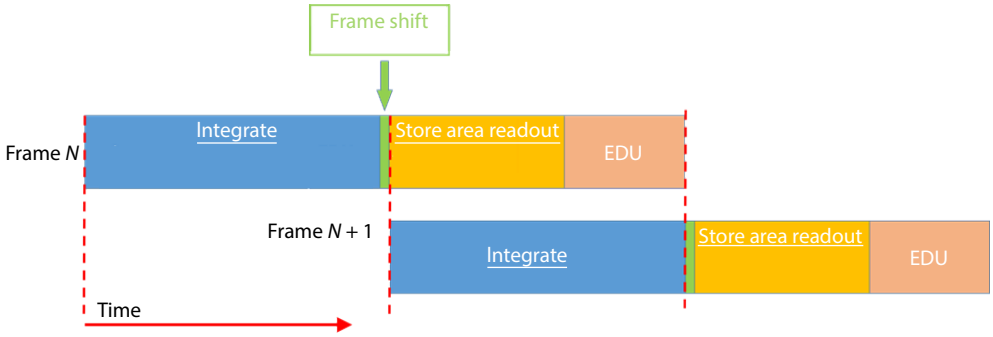

Figure 4. Flight-like frame transfer readout.

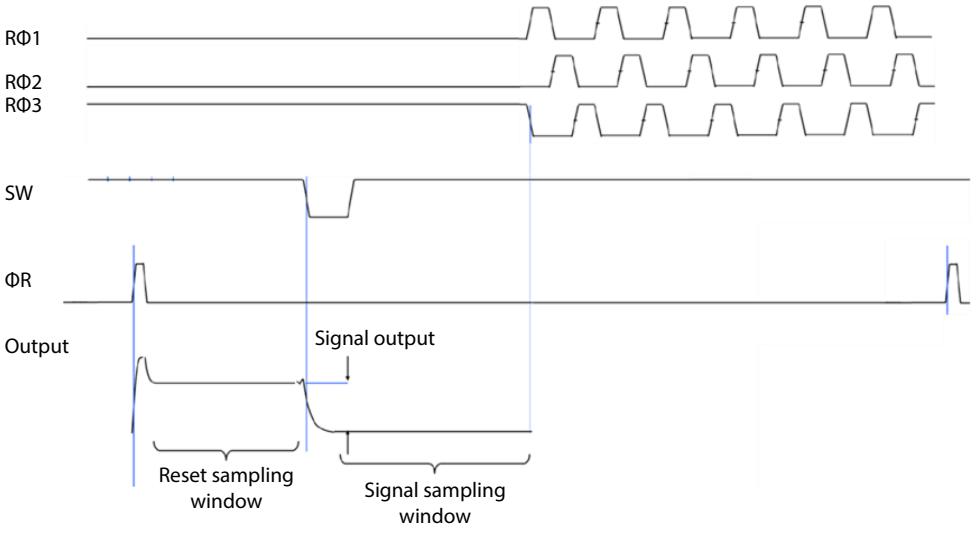

Figure 5. Output and register clocking with 6 × 6 binning onto the summing well in burst mode where RΦ 1–3 = serial clocks, SW = summing well and ΦR = reset.

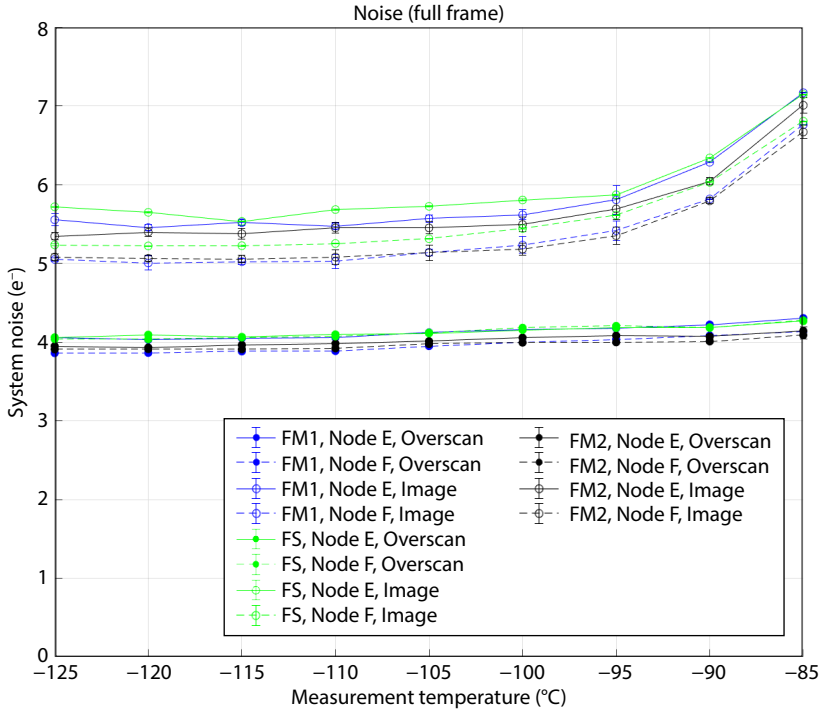

Figure 6. System noise on both nodes in the CCDs across tested temperature range while readout is in full frame mode. The error on each data point is the standard error from a Gaussian fit to the noise peak.

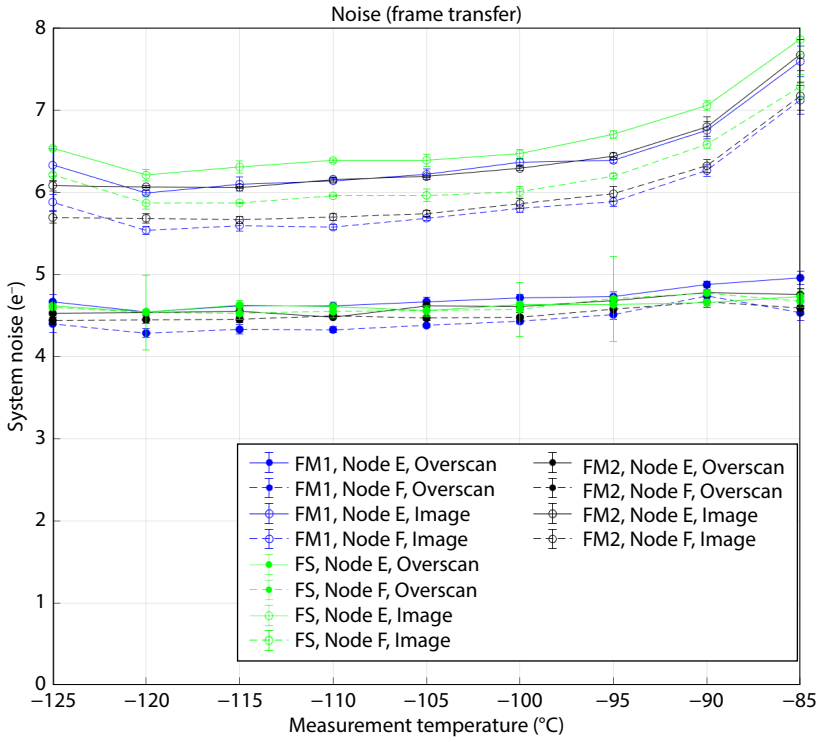

Figure 7. System noise on both nodes in the CCDs across tested temperature range while readout is in frame transfer mode. The error on each data point is the standard error from a Gaussian fit to the noise peak.

temperature or device and remains approximately at or below 150 eV for both full frame (Figure 8) and frame transfer readouts (Figure 9). There is a slight increase in FWHM at −125 °C; however this is thought to be a test system issue rather than a device characteristic, as the same behaviour is not seen in the OU's similar setups with engineering model CCD370s. The Fano limit and the Fano plus readout noise spectral resolution have been added to both plots. An example of the Fe-55 spectra used to measure the FWHM, with the associated Gaussian fits, is shown in Figure 10 for both full frame and frame transfer readouts. The jagged structures in the spectra are due to the analogue-to-digital conversion limits in the electronics.

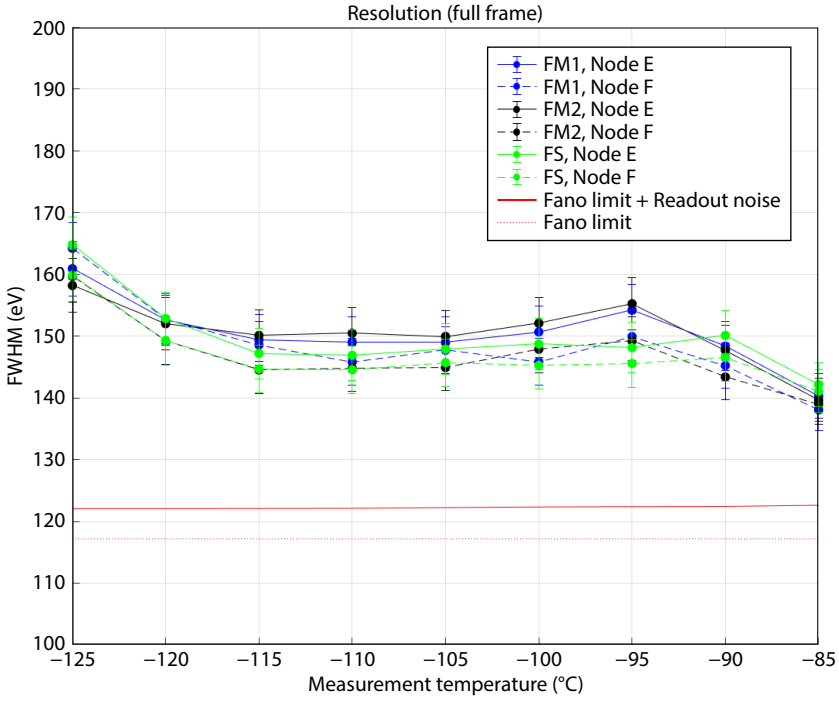

Figure 8. Full frame FWHM of 5.9 keV Fe-55 Kα photopeak across temperature range; the error on each data point is the standard error.

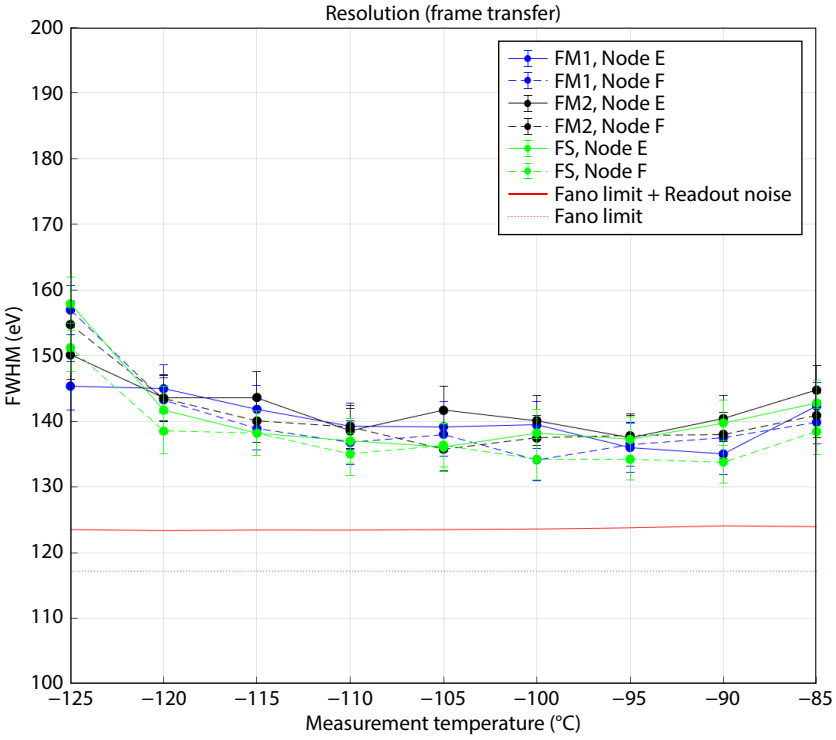

Figure 9. Frame transfer FWHM of 5.9 keV Fe-55 Kα photopeak across temperature range; the error on each data point is the standard error.

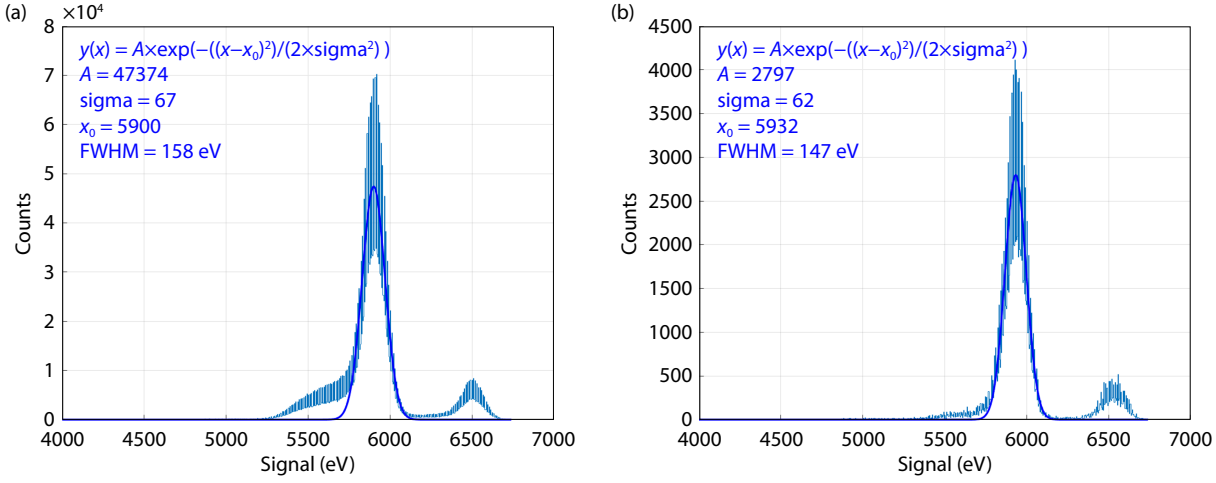

Figure 10. Fe-55 spectra at −120 °C for (a) Full frame and (b) Frame transfer readout modes, only isolated X-rays are plotted (those where over 90% of the signal is in one pixel).

3.3 Dark Current

The dark current (DC) is calculated as a median value across the image area in each node of the devices by plotting the signal in e^{-}·pix^{-1} for the integration times (5, 300, 900, 1800, 3600 s) and extracting the gradient. 30 minute and 1 hour integration times have been used in the full frame measurements to get the DC readings at the lowest temperatures, as accurate as possible.

The procurement reference is CCD-DRK-001-A, which states that the average dark signal at −70 °C and 0 Volt substrate voltage shall be lower or equal to 1.2 e^{-}·pix^{-1}·s^{-1} at BOL (*SMILE CCD procurement specifications*, 2017).

The results in Figure 11 show that the dark current gradually increases with temperature; however the linearity is lost in the full frame data below −105 °C due to the DC being so low that it falls below the noise floor of the measurements. At the nominal −120 °C operating temperature the full frame DC is 1×10^{-3} e^{-}·pix^{-1}·s^{-1} for all devices when reading directly from the figure, and 5×10^{-5} e^{-}·pix^{-1}·s^{-1} when extrapolating from the linear section of the figure. The frame transfer DC is easier to measure, as 36 native pixels are binned together, which improves the signal to noise ratio. At operating temperature the DC across all devices is 1.5×10^{-3} e^{-}·pix^{-1}·s^{-1}, which matches well with the native pixel extrapolated result (1.5×10^{-3} /36 = 4.2×10^{-5}).

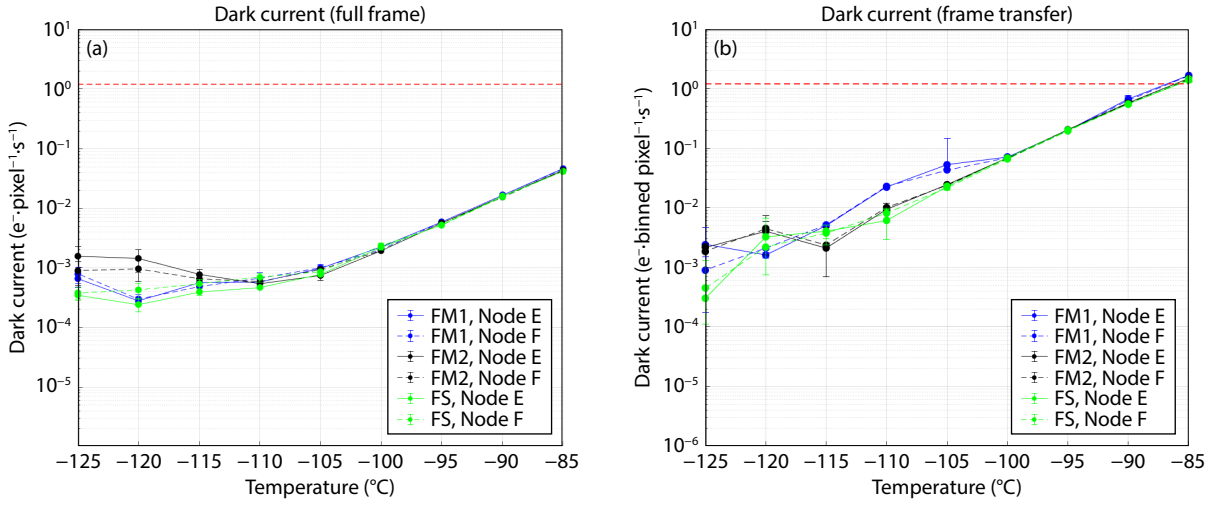

Figure 11. Dark Current in native pixel full frame (a) and Dark Current 6 x 6 binned frame transfer (b) mode across −125 to −85 °C, the error on each data point is calculated by combining the standard error from each integration time. Note that *Y* scale is in e⁻·binned pixel^{-1}·s^{-1} in (b).

The procurement specification of 1.2 e⁻·pix^{-1}·s^{-1} is based on a measurement temperature of −70 °C which is outside the tested range and significantly warmer than the nominal operating temperature. The full frame result may well meet this requirement but the frame transfer will not. The DC performance at the nominal operating temperature, however, easily meets the 1.2 e⁻·pix^{-1}·s^{-1} requirement.

3.4 Bright Defects

The number of bright defects is measured throughout the temperature range. A bright defect is classified as a native pixel exhibiting a signal greater or equal to 10 e⁻·pix^{-1}·s^{-1}. Where a hot column is present, the individual hot pixels within it are not counted.

The procurement reference is CCD-DEF-003-A which states that the total number of bright pixels shall be lower than 600 at BOL at −70 °C.

At the nominal operating temperature any bright pixels present are within the 600 pixel threshold; in FM1 and FM2 there are not any below −105 °C, Figure 12.

However in Node F of the FS there is a cluster of hot pixels, illustrated in Figure 13, which gradually increases with temperature until it crosses the threshold at −100 °C. At the highest tested temperatures two hot columns also formed with the source, likely to be the hot pixel cluster.

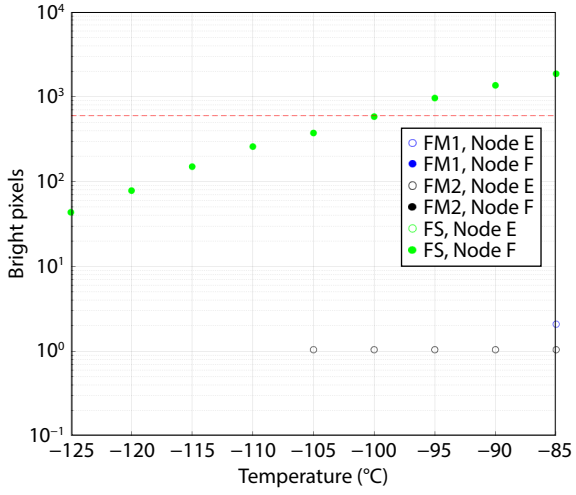

Figure 12. Number of bright pixels found in the CCD370s above the 10 e⁻·pix^{-1}·s^{-1} threshold.

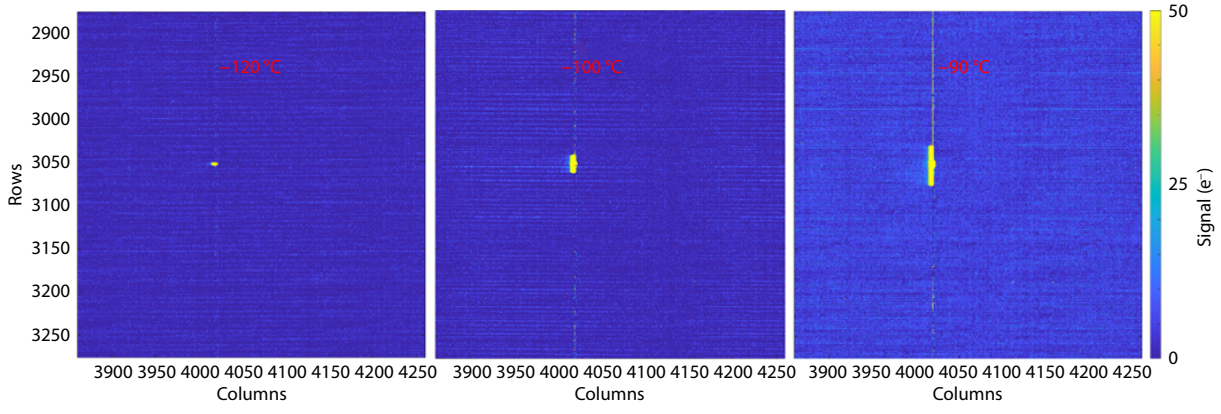

Figure 13. Development, with temperature, of a cluster of hot pixels in Node F of FS.

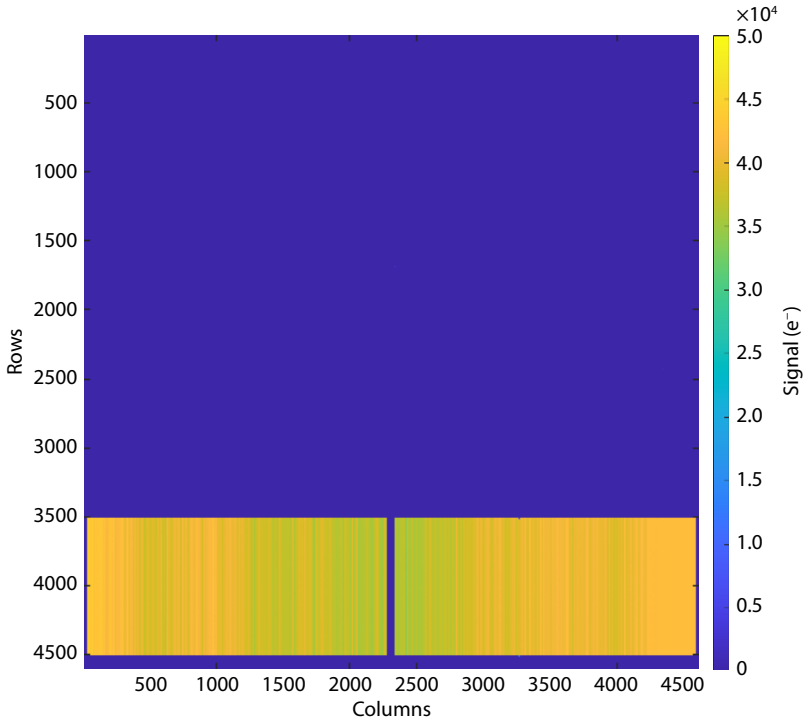

Figure 14. Full frame image at −110 °C with 40 ke⁻ injected into the last 1000 rows to create edges at which EPER can be measured.

3.5 Assessment of the Charge Injection Structure's Uniformity

Charge injection (CI) uniformity has been assessed by varying the injected signal level using the guard drain voltage (V_{GD}) across the temperature range. The isolation gate voltage (V_{IG}) has been set for each signal level to provide optimum uniformity. The median noise along the rows and down the columns is presented.

There are no procurement specifications relating to the charge injection uniformity; however the estimated Shot noise is displayed alongside the results as a point of reference.

Charge injection images such as that in Figure 14 were taken and the row-row/column-column variation in signal size assessed.

Figure 15a–c show how the signal uniformity varies across the columns, with higher signal towards the outer edges and lower variation across the structure at smaller signal levels.

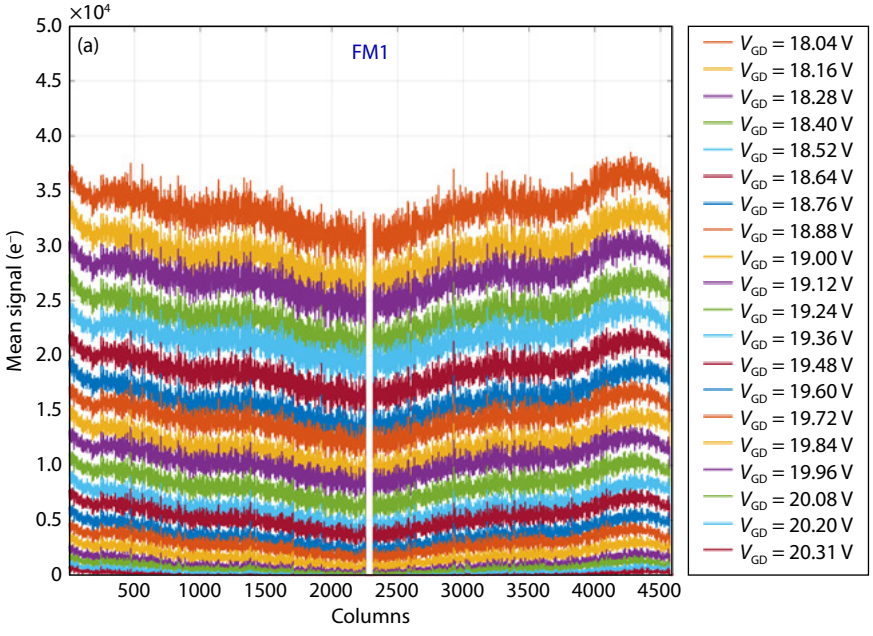

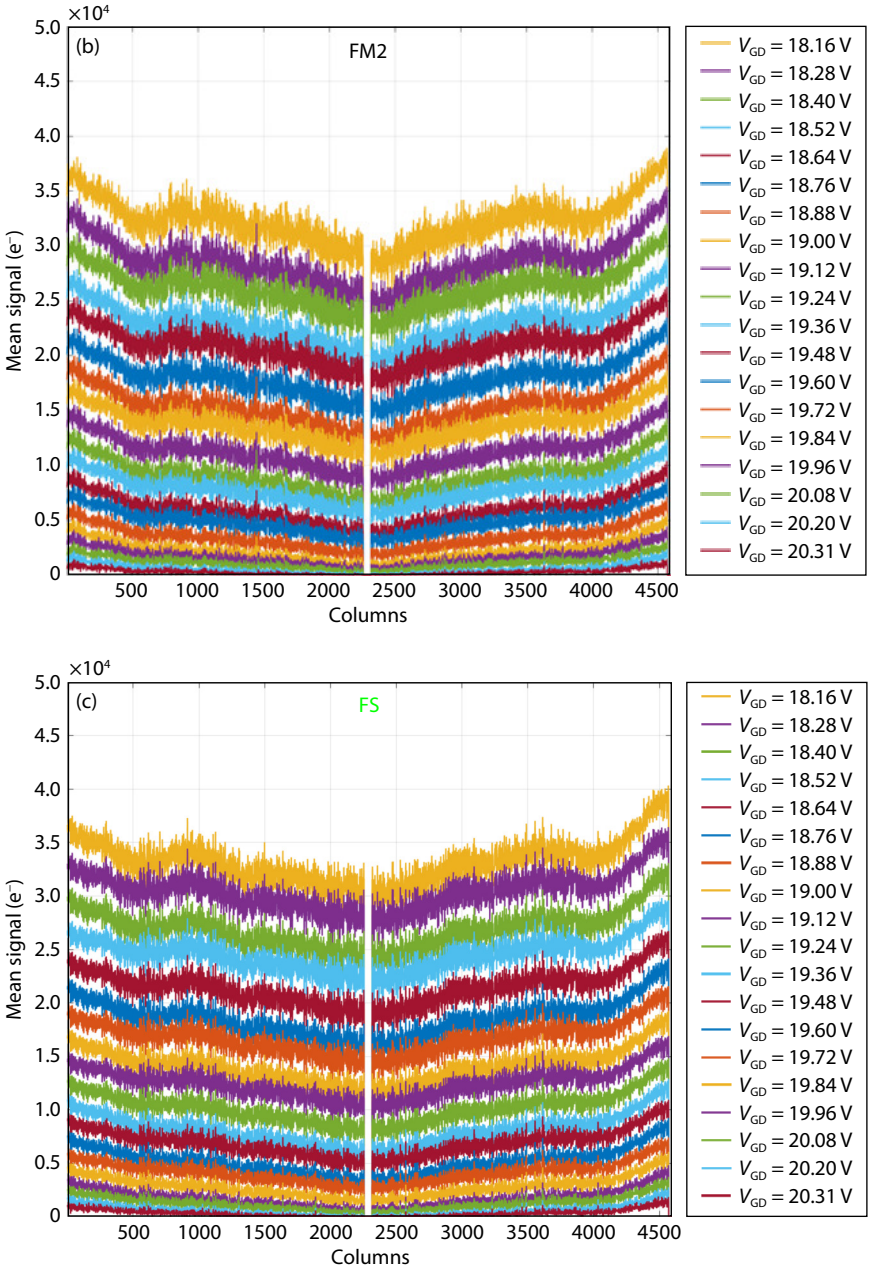

Figure 15. FM1 (a), FM2 (b), and FS (c) CI uniformity across columns for different signal levels at −120 °C.

The increase in non-uniformity with signal level is shown in Figure 16. This has been calculated by measuring the standard deviation of the injected charge in each column/row and then taking the median of that value over a range of signal levels and temperatures. The dashed line in each plot is the square root of the injected signal size and provides an estimation of the Shot noise at each signal level. The error on each data point is the standard error and is calculated from the standard deviation of the signal levels.

The intercolumn (vertical) noise is very low and sits below the predicted Shot noise; however, the column-to-column (horizontal) noise is significantly higher as each column has an individual injection structure which varies slightly. This therefore means that the actual amount of charge being put in changes from column to column, but that level is very stable.

3.6 Trap Pumping

To assess the number of traps present in each device, trap pumping has been carried out using charge injection to input signal into the image. The testing has been focussed around the emission times that will have the largest effect on the CTI at the selected operating speeds and temperatures. As a result, emission that are based around the divacancy and towards the unknown defect will be probed. Ideally, slower defects would also have been probed; however, due to tight scheduling requirements, quicker emission time constants were the focus of the work presented here. Each pixel has four electrodes that alternate in width between 4 to 5 μm, the parallel trap pumping mode used probes half of a 4 μm and half of a 5 μm; effectively 1/4 of each pixel. This assumes that the traps under 1/4 of each pixel are identical to those in the remaining 3/4, which is a reasonable assumption and saves an

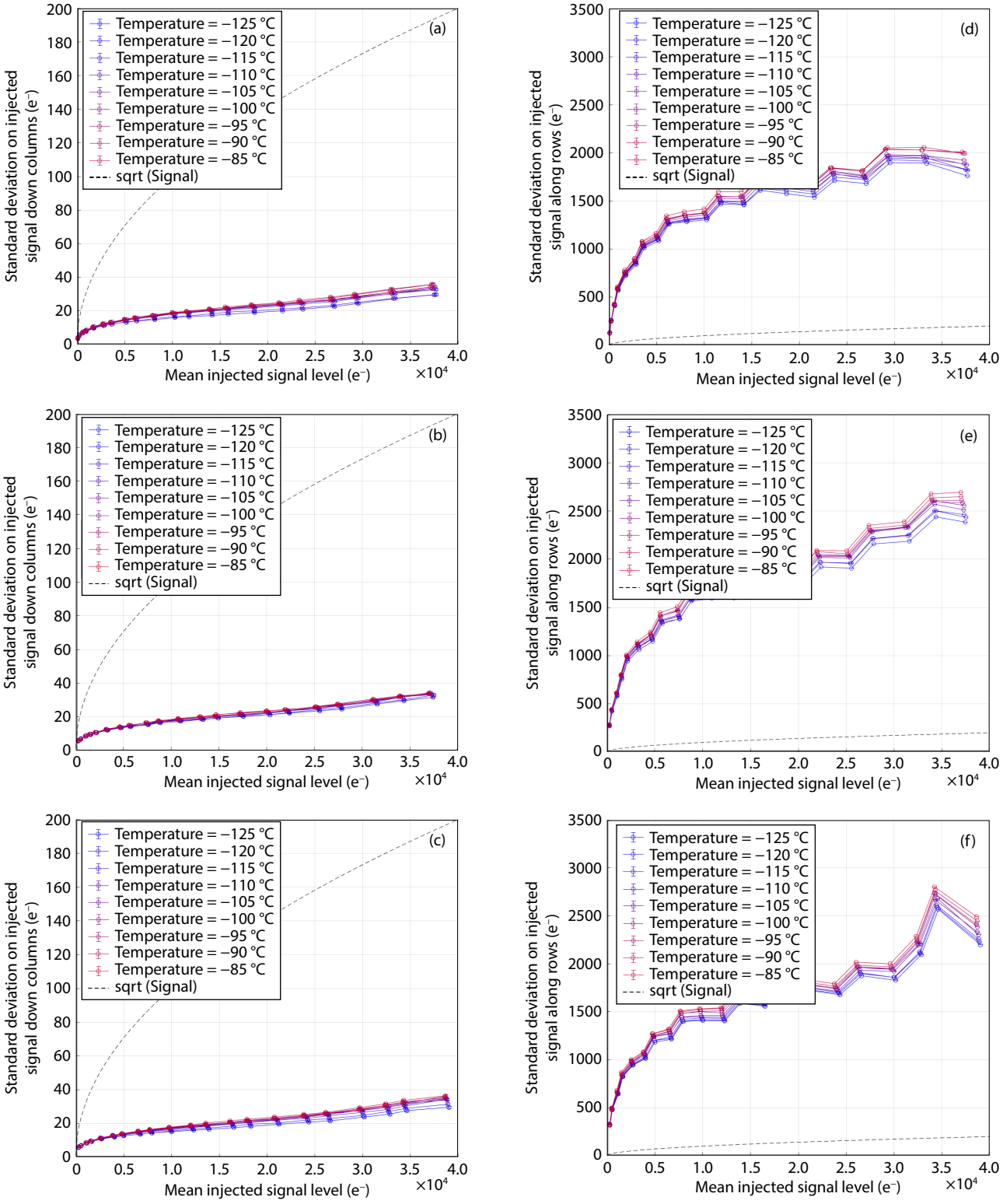

Figure 16. (a, b, c) FM1, FM2, and FS mean noise down columns at varying signal levels across the temperature range, corrected for CTI noise. (d, e, f) FM1, FM2, and FS mean noise along rows at varying signal levels across the temperature range, corrected for CTI noise. The deviation is more steplike in the row results due to the optimised voltage settings being set based on the row uniformity.

additional factor of 4 with respect to time for data acquisition. Results are presented as number of traps per pixel (based on the assumption above), for simplicity.

There are no procurement specifications explicitly relating to the number and types of traps present in each device; however, it is intrinsically linked to the CTI.

The results in Figure 17a–c show the trap landscapes of FM1, FM2, and FS at −125 °C, −115 °C, and −100 °C, respectively. All three

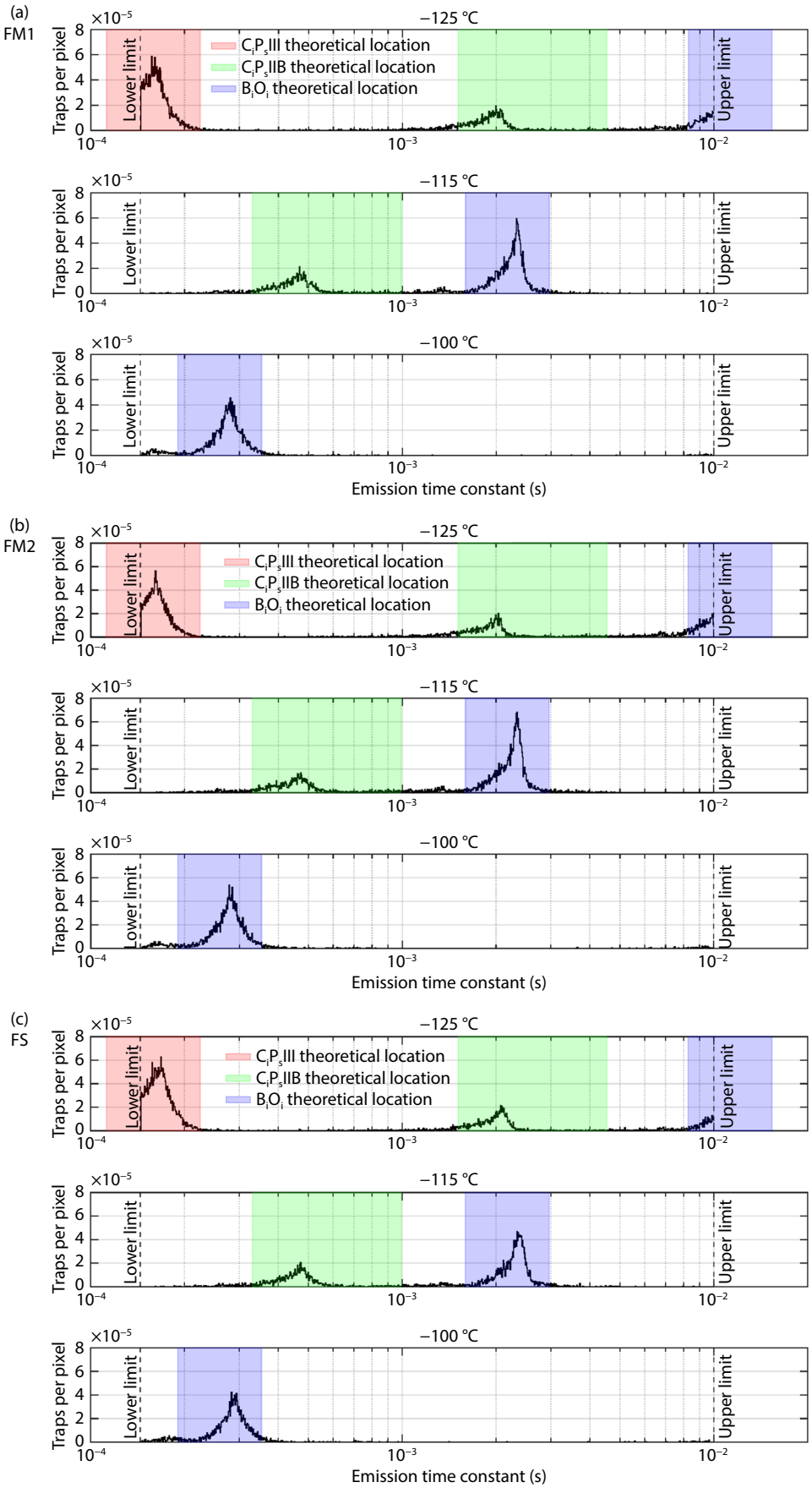

Figure 17. Trap landscapes of the FM1 (a), FM2 (b), and FS (c) at the three coldest temperatures.

devices show similar trap distributions, with 3 main peaks present across each of the devices. These peaks are most likely intrinsic manufacturing defects, which are inherently present in the silicon, and can be attributed to a mixture of carbon, phosphorous, boron, and oxygen. The theoretical locations for three specific manufacturing defects, two atomic configurations of the carbon phosphorous complex (CiPs ||| and CiPs ||B), and a boron-oxygen complex (BiOi), are shown in the red, green, and blue color ranges. Small changes in cross section and energy level mean that the peak emission time constant location of the defect in question can change, but the peak should be in the range stated. All three manufacturing defects present in the devices here have been found in recent comprehensive studies (Bush et al., 2021), and the emission time constants locations across the temperature ranges show good agreement.

The density of each manufacturing defect is also relatively low (when compared to defect densities of radiation-induced traps), and this low defect density is also corroborated by the low levels of CTI seen in Figures 18, 19, 20. After irradiation, it is expected that the density of the manufacturing defects seen pre-irradiation, will be insignificant compared to the density of radiation-induced defects, such as the divacancy, unknown, phosphorous vacancy, and oxygen vacancy.

Temperature −85 °C was not included as there were no defects with significant densities found within this parameter space (as expected). As shown in Figure 17, the emission time constant of the three main manufacturing defects present are moving out of the emission time constant range probed, and thus cannot be probed at −85 °C.

3.7 Charge Transfer Inefficiency – X-ray

The most accurate way to predict the effects of CTI on the SXI during the SMILE mission is to take images with X-rays and measure how the signal size varies across the image area due to transfer losses. The parallel and serial CTI (pCTI/sCTI) for frame transfer and un-binned full frame readout have been measured. The same method as described in (Parsons et al., 2021) is used with integration times of 300 s for the full frame images and 10 s for frame transfer, to provide X-ray densities of 1 per 220 native pixels and 1 per 1500 binned pixels, respectively. Errors are calculated from the residuals of the non-linear CTI fit function.

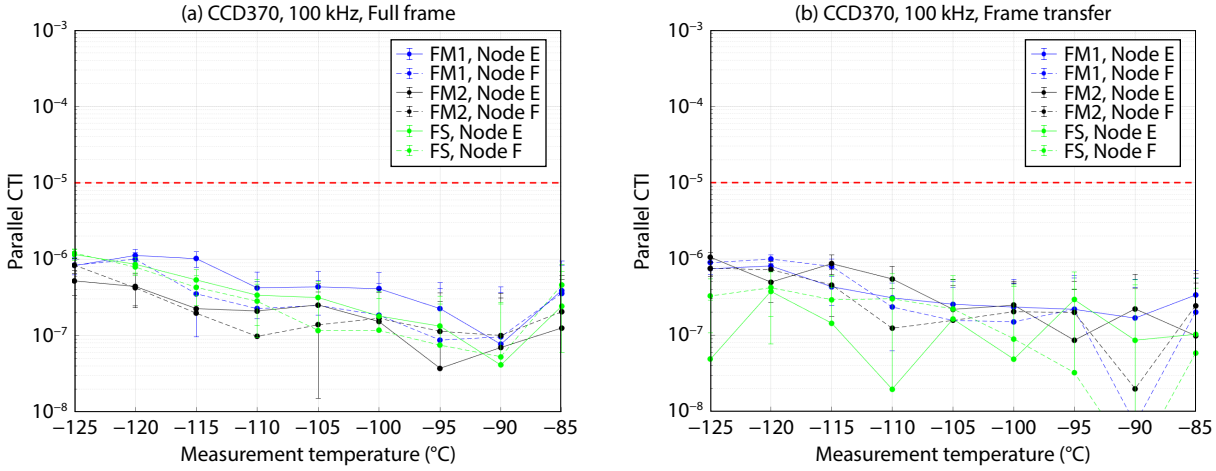

Figure 18. Parallel X-ray CTI in FT mode for FM1, FM2, and the FS.

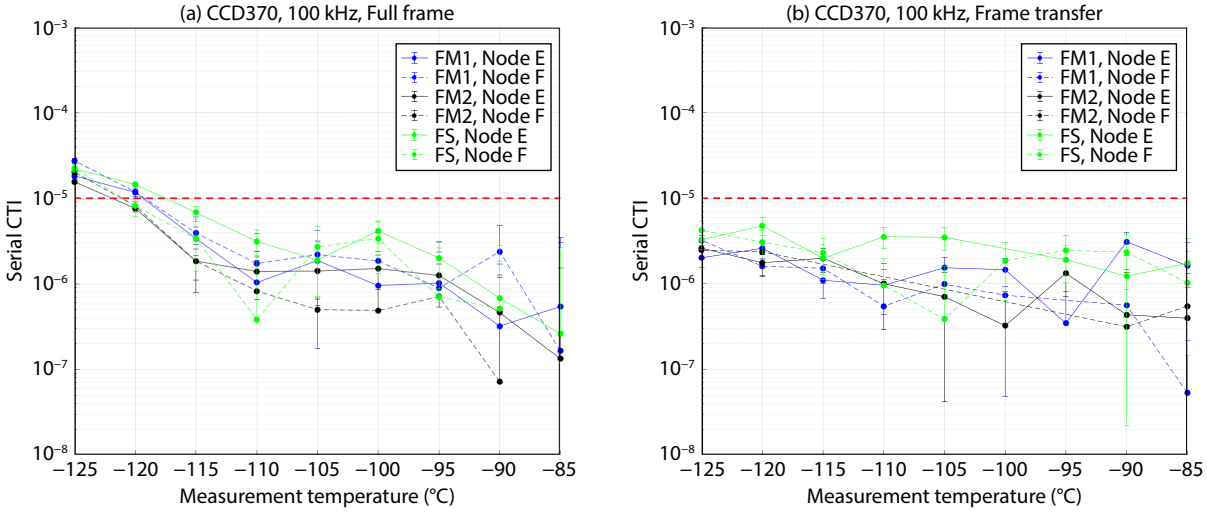

Figure 19. Serial X-ray CTI in FT mode for FM1, FM2, and the FS.

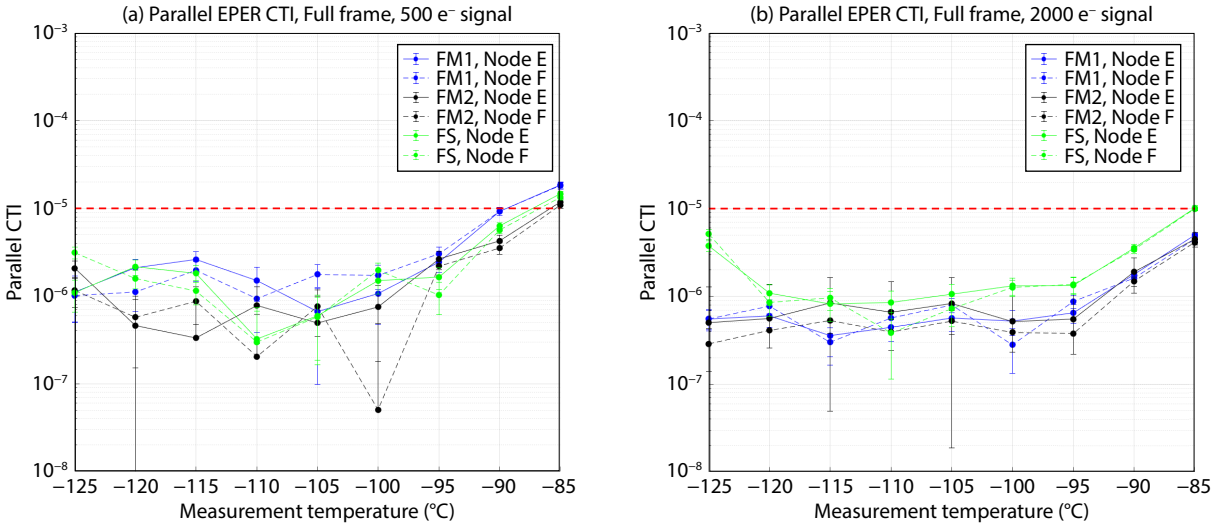

Figure 20. Parallel EPER CTI with 500 e⁻ (a) and 2000 e⁻ (b) injected signal for FM1, FM2, and the FS.

The procurement reference for parallel CTI is CCD-CTE-001-A. It states that the charge transfer efficiency in the parallel direction shall be higher or equal to 99.999 % (CTI $\leq 1 \times 10^{-5}$) at BOL. For serial CTI the reference is CCD-CTE-001-A and states that the charge transfer efficiency in the serial direction shall be higher or equal to 99.999 % (CTI $\leq 1 \times 10^{-5}$) at BOL. These specifications are based on using an Fe-55 source; therefore the corresponding signal level is 1611 electrons.

The pCTI is measured for all the devices with the full frame results in Figure 18a and the frame transfer results in Figure 18b, showing that it stays constant within error at $<1 \times 10^{-6}$, which is significantly better than the 1×10^{-5} in the procurement specifications and does not vary significantly between CCDs.

The sCTI in Figure 19a and b shows that it does improve with temperature, in agreement with the EPER sCTI results. In full frame mode the sCTI is higher than the threshold at the coldest temperatures; however, this is not the case in frame transfer where the charge tails are collected by the binning. The procurement specification is assumed to be based on science mode operations, which are binned frame transfer therefore the results are compliant.

3.8 Charge Transfer Inefficiency – Extended Pixel Edge Response

The CTI is also calculated using the EPER, which measures the emission of charge from traps. The pCTI and serial CTI (sCTI) for full frame readout is presented. Frame transfer data were not taken as a combination of the charge injection uniformity; 6×6 binning caused saturation in the readout electronics. Measurements have been made over two charge levels, corresponding to the Fe-55 (1600 e⁻) and the approximate science (500 e⁻) signal level; the injected charge level is calculated by taking the mean signal. The error on each data point is the standard error and is calculated from the standard deviation of the signal levels in the charge tail. The EPER measurements have be made using images containing 1000 lines of injected charge followed by 300 pixels of overscan.

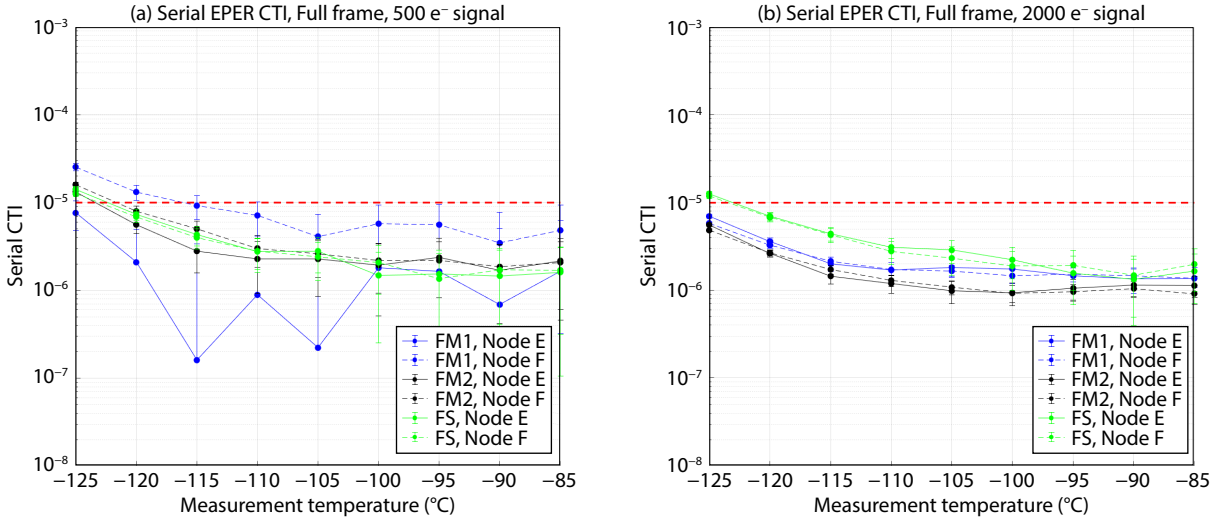

Figure 21. Serial EPER CTI with 500 e⁻ (a) and 2000 e⁻ (b) injected signal for FM1, FM2, and the FS.

The procurement specification is the same for EPER CTI as that for the X-ray CTI in Section 3.7.

The results in Figure 20a and Figure 20b show that EPER pCTI largely agrees with the X-ray pCTI results. However, above −100 °C the CTI starts to increase above the threshold in a way that is not seen in the X-ray results. This difference is thought to be due to EPER not measuring trap capture, and, as the temperature increases, one or more of the traps present starts to dominate the CTI with its emission.

The results in Figure 21a and Figure 21b show that the serial EPER CTI appears to improve with temperature and has similar values to the X-ray sCTI.

In Figure 21a the FM1 data (blue) has significantly larger error bars than the other devices. This has been caused by an insufficiently high signal level being used for the measurement, due to slight variations between devices. This has meant that the final few columns of charge injection are a lot lower than expected, giving spurious results. However, within error the results are very similar across the 3 CCDs.

4. Summary

A baseline characterisation of the SMILE SXI flight CCDs was performed and the results were compared against the procurement specifications. The results show that the performance of all three devices is very high and easily meet the specifications for the nominal −120 °C operating temperature when running in 6 x 6 binned frame transfer science mode. The sCTI results show that performance degrades as temperatures decrease when in full frame mode; however, binning/frame transfer reduces the effect to the point where sCTI is largely independent of temperature. The planned CCD370 radiation damage campaign will help clarify whether this behavior is likely to continue throughout the mission.

There is, however, a cluster of bright pixels in Node F of the FS that changes with temperature, such that, if the specification is followed (< 600 bright pixels at −70 °C), it fails but at the operating temperature it passes.

Further testing is currently being carried out using the flight spare to get X-ray results from a variety of different fluorescence targets with characteristic X-rays in the SXI's science band.

Acknowledgments

This work was supported by the following grants: SMILE 2019–2022 STFC (Grant reference: ST/T003138/1); SMILE 2022–2023 ESA (Contract No: 4000138219/22/NL/BW/pbe).

References

Bush, N., Hall, D., and Holland, A. (2021). Proton-induced traps in electron multiplying charge-coupled devices. *J. Astron. Telesc. Instrum. Syst.*, *7*(1), 016003. https://doi.org/10.1117/1.JATIS.7.1.016003

Clarke, A. S., Hall, D. J., Holland, A., and Burt, D. (2012). Modelling charge storage in Euclid CCD structures. *J. Instrum.*, *7*(1), C01058. https://doi.org/10.1088/1748-0221/7/01/C01058

Dennerl, K., Lisse, C. M., Bhardwaj, A., Christian, D. J., Wolk, S. J., Bodewits, D., Zurbuchen, T. H., Combi, M., and Lepri, S. (2012). Solar system X-rays from charge exchange processes. *Astron. Nachr.*, *333*(4), 324. https://doi.org/10.1002/asna.201211663

Endicott, J., Walker, A., Bowring, S., Turner, P., Allen, D., Piersanti, O., Short, A., and Walton, D. (2012). Charge-coupled devices for the ESA PLATO M-class mission. In *Proceedings of the SPIE 8453, High Energy, Optical, and Infrared Detectors for Astronomy V* (pp. 84531J). Amsterdam, Netherlands: SPIE. https://doi.org/10.1117/12.926299

Pagani, C., Beardmore, A. P., Abbey, A. F., Mountford, C., Osborne, J. P., Capalbi, M., Perri, M., Angelini, L., Burrows, D. N., … Starling, R. L. C. (2011). Recovering Swift-XRT energy resolution through CCD charge trap mapping. *Astron. Astrophys.*, *534*, A20. https://doi.org/10.1051/0004-6361/201117660

Parsons, S., Buggey, T., Holland, A., Sembay, S., Randall, G., Hetherington, O., Yeoman, O., Hall, D., Verhoeve, P., and Soman, M. (2021). Effects of temperature anneal cycling on a cryogenically proton irradiated CCD. *J. Instrum.*, *16*(11), P11005. https://doi.org/10.1088/1748-0221/16/11/p11005

Raab, W., Branduardi-Raymont, G., Wang, C., Dai, L., Donovan, E., Enno, G., Escoubet, P., Holland, A., Jing, L., … Wielders, A. (2016). SMILE: a joint ESA/CAS mission to investigate the interaction between the solar wind and earth's magnetosphere. In *Proceedings of the SPIE 9905, Space Telescopes and Instrumentation 2016: Ultraviolet to Gamma Ray* (pp. 990502). Edinburgh, UK: SPIE. https://doi.org/10.1117/12.2231984

Seabroke, G. M., Prod'homme, T., Murray, N. J., Crowley, C., Hopkinson, G., Brown, A. G. A., Kohley, R., and Holland, A. (2013). Digging supplementary buried channels: investigating the notch architecture within the CCD pixels on ESA's Gaia satellite. *Mon. Not. R. Astron. Soc.*, *430*(4), 3155–3170. https://doi.org/10.1093/mnras/stt121

Walsh, B. M., Collier, M. R., Kuntz, K. D., Porter, F. S., Sibeck, D. G., Snowden, S. L., Carter, J. A., Collado-Vega, Y., Connor, H. K., … Thomas, N. E. (2016). Wide field-of-view soft X-ray imaging for solar wind-magnetosphere interactions. *J. Geophys. Res.: Space Phys.*, *121*(4), 3353–3361. https://doi.org/10.1002/2016JA022348